RESEARCH ARTICLE

Theoretical and experimental analysis of negative dielectrophoresis-induced particle trajectories

Ramona Luna[1,2] ⓘ | **Daniel P. Heineck**[1] ⓘ | **Elmar Bucher**[2] ⓘ | **Laura Heiser**[2] ⓘ |
Stuart D. Ibsen[1,2] ⓘ

[1]Cancer Early Detection Advanced Research Center, Knight Cancer Institute, Oregon Health and Science University, Portland, Oregon, USA

[2]Department of Biomedical Engineering, School of Medicine, Oregon Health and Science University, Portland, Oregon, USA

Correspondence
Stuart Ibsen, Cancer Early Detection Advanced Research Center, Knight Cancer Institute, Oregon Health and Science University, Portland, OR 97201, USA.
Email: ibsen@ohsu.edu

Color online: See article online to view Figures 1–5 in color.

Abstract
Many biomedical analysis applications require trapping and manipulating single cells and cell clusters within microfluidic devices. Dielectrophoresis (DEP) is a label-free technique that can achieve flexible cell trapping, without physical barriers, using electric field gradients created in the device by an electrode microarray. Little is known about how fluid flow forces created by the electrodes, such as thermally driven convection and electroosmosis, affect DEP-based cell capture under high conductance media conditions that simulate physiologically relevant fluids such as blood or plasma. Here, we compare theoretical trajectories of particles under the influence of negative DEP (nDEP) with observed trajectories of real particles in a high conductance buffer. We used 10-μm diameter polystyrene beads as model cells and tracked their trajectories in the DEP microfluidic chip. The theoretical nDEP trajectories were in close agreement with the observed particle behavior. This agreement indicates that the movement of the particles was highly dominated by the DEP force and that contributions from thermal- and electroosmotic-driven flows were negligible under these experimental conditions. The analysis protocol developed here offers a strategy that can be applied to future studies with different applied voltages, frequencies, conductivities, and polarization properties of the targeted particles and surrounding medium. These findings motivate further DEP device development to manipulate particle trajectories for trapping applications.

KEYWORDS
dielectrophoresis, electric field model validation, lab-on-chip, particle tracking

---

Abbreviations: FEM, finite element method; nDEP, negative dielectrophoresis; pDEP, positive dielectrophoresis.

- -

1 | INTRODUCTION

The ability to capture cells of interest at specific locations within microfluidic chips is essential for many biomedical analysis applications. These cellular trapping techniques can separate individual cells from one another, enabling the analysis of single-cell behavior and physical characteristics [1, 2]. Trapping cells in precise locations within microfluidic chambers also enables the study of the impact of different environmental factors on cell behavior, including exposure to gradients of therapeutic drugs and signaling factors created within the fluidic system [1, 3]. Clustering just a few cells together in separate groups also enables the study of cell interactions with one another [4], including the formation of organoid-like structures [5]. Trapping cells within the sample can also be used as a separation mechanism for the purification of cells from other particles in the media. For example, moving cells in a blood sample to specific locations within the fluidic device is essential to separate them from circulating nanoparticles to enable nanoparticle analysis. This is important for the study of extracellular vesicles, including exosomes, which carry important disease-related biomarkers, including biomarkers for cancer [6–9, 10].

Precisely manipulating the location of cells within microfluidic devices remains a challenge due to their small size and the small fluid volume within the chambers. Various trapping methods have been developed to achieve cellular separations and manipulations [1]. These are based on physical trapping methods of the cells either through the formation of specialized trapping structures [11, 12], or the manipulation of fluid flow to trap cells at constriction points within the devices [13]. Patterning various binders to the surface of the chips can also result in individual cells or groups of cells being trapped in desired locations [14]. Continuous flow separation strategies that use physical barriers to cause cell separations have also been developed [15], but under these flow conditions it is difficult to study cellular interactions or environmental effects on cellular behavior. These physical barriers, traps, and binding agents that capture cells under flow put various mechanical stresses on the cells that can cause changes in genetic expression and behavior [16–18]. The continuous fluid flow patterns that these techniques require also make it difficult to analyze untrapped nanoparticles in the sample.

One promising method to achieve precise spatial manipulation and trapping of cells within a microfluidic device without the use of physical barriers, binding agents, or bulk fluid flow is dielectrophoresis (DEP). This label-free trapping method relies on the differences between the dielectric properties of the cell and the surrounding media [19, 20, 22]. An applied external electric field induces a dipole in the cell that will subsequently experience a force if the applied electric field is nonuniform [23]. The DEP force that a homogenous spherical entity experiences is defined by the following equation:

$$F_{DEP} = 2\pi r^3 \varepsilon_o \varepsilon_m \left[CM \right] \nabla |\boldsymbol{E}|^2 \qquad (1)$$

where r is the radius of the particle, ε_o is the permittivity constant for vacuum, ε_m is the permittivity constant for the medium, CM is the frequency-dependent Clausius–Mossotti factor relating to the polarizability of the particle and medium, and $\boldsymbol{E}$ is the applied electric field [23].

This expression indicates that the magnitude of the DEP force exerted on the particle depends on the electric field gradient. The direction of particle movement will either follow the electric field gradient toward the high-field regions, known as positive DEP (pDEP), or be repelled toward the low-field regions, known as negative DEP (nDEP). The distinction between pDEP and nDEP is dictated by the CM sign, which is frequency dependent.

As microfabrication techniques have evolved, contemporary technology now allows for the fabrication of micro-sized electrodes that can be incorporated into lab-on-chip devices to create the nonuniform electric fields necessary for DEP [20]. As the size of the electrodes is reduced, a lower voltage is required to create electric fields with sufficient gradients to manipulate cells and nanosized particles such as exosomes [20–22, 24–28]. These electrode arrays can be designed to create nonuniform electric fields with high- and low-intensity regions in desired locations across the microfluidic chamber, creating specific places where cells can be trapped under static fluid conditions. DEP has also been applied to continuous flow systems for the separation of different cell types. Cell mixtures are flowed over specially designed electrode array geometries, and the DEP forces induced upon the cells by the nonuniform electric field cause them to levitate at different heights above the array. The height of levitation is dependent on the cell's dielectric properties that affect the magnitude of the nDEP force experienced. Different cell types reach different heights and can then be collected separately [29–35].

In our case, we are using chips that have an array of circular microelectrodes at the bottom of the chip that create high-field regions around the electrode edge and low-field regions in between electrodes (Figure 1). This particular electrode array configuration can create nDEP forces that are strong enough on cell-sized particles to take them all the way to the global minima where trapping occurs. The schematics in Figure 1A–C show a cross-sectional view of the DEP chips with flat planar electrodes. A protective hydrogel layer covering the electrodes was used to reduce electrochemistry and bubble formation [27, 36]. This unique feature enabled these chips to successfully
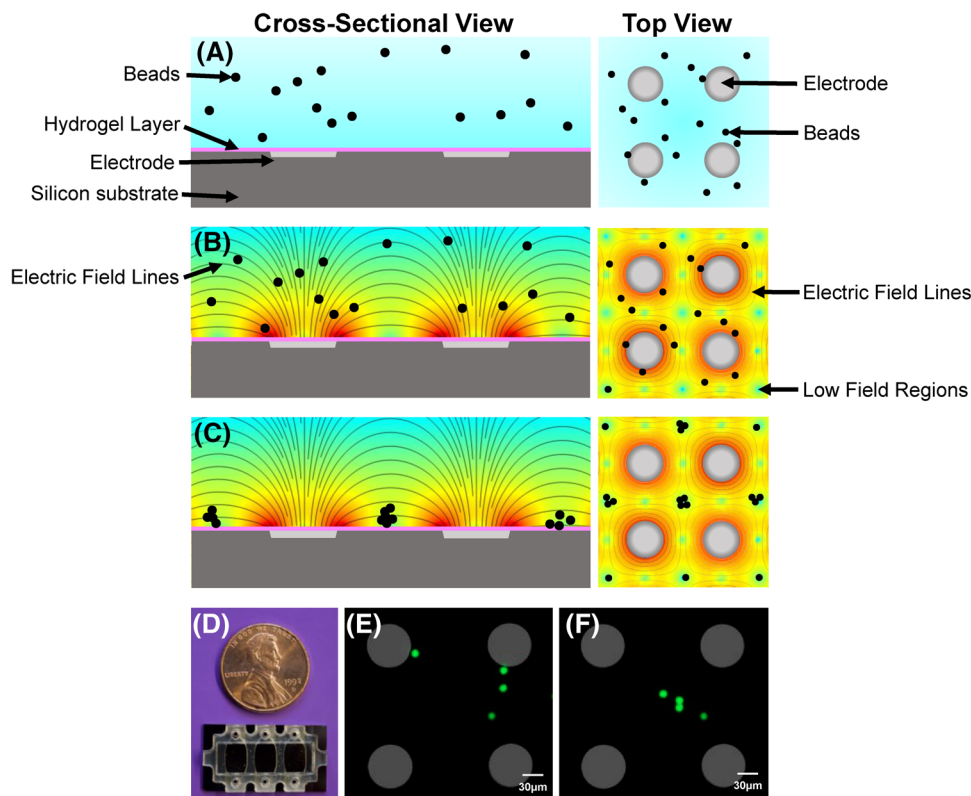
FIGURE 1 Collection of polystyrene beads under nDEP conditions. (A) A schematic representation of the DEP chip in both cross-sectional and top views before electric field application. (B) The AC electric field is applied to generate nDEP. The black lines in the cross-sectional view are the electric field lines created between electrodes. The red coloration represents the high-field regions and light blue the low-field regions. (C) After 40 s of DEP, the particles are collected in the low-field regions between the electrodes. (D) Photograph showing the Biological Dynamics DEP chips used for this study next to a penny that is 19 mm in diameter. (E) A fluorescent image of the 10-μm yellow–green fluorescent beads has been overlaid on a corresponding bright-field image of four circular electrodes within the array. They were at their random initial locations before DEP was applied. (F) After 40 s of AC electric field application, the particles moved under the influence of nDEP and were trapped in the low-field region between the electrodes. AC, alternating current; DEP, dielectrophoresis; nDEP, negative DEP

apply the electric field to high conductance media such as undiluted human blood and plasma [36, 37]. Here we modeled physiological fluids using high conductance 0.5× phosphate-buffered saline (PBS) containing 10-μm diameter polystyrene beads. The blue regions in the top view schematics represent the local minima of the electric field directly between two electrodes and global minima in the center among four electrodes. One of the advantages of nDEP is that it results in a contactless isolation of particles (Figure 1E and F) through the formation of nDEP cages or traps, providing stable collection with applications including the manipulation of single cells [38, 39].

In order to optimize the trapping of cells on the chip, it is nessesary to further understandthe effects of DEP and other chip-generated forces on cell collection. It has been reported that Joule heating of the electrodes can introduce confounding effects during DEP experiments [22, 40–43]. The production of a temperature gradient, due to heating of the electrodes at the bottom of the fluidic

chamber, can create localized buoyancy-driven convection of the media [44–47]. Furthermore, at certain voltages and frequencies, corrosion of the electrodes can occur in high-conductivity media [37]. Some of this heating can be mitigated by varying the geometry of electrodes [38, 48], the material used for fabrication of electrode arrays [49], and ultimately, the DEP voltage and frequencies applied according to the samples that will be used and the targeted particles. However, the development of thermally driven convection cells on these chips is unavoidable. Another electric field–induced fluid motion that could be occurring is electroosmosis and the effects of this can add to the thermal flow [50–54]. Although electroosmosis has been used as a particle separation method aid, it is unknown how these currents might affect the nDEP-based collection of cells under high conductance conditions. The relative effects of DEP forces, thermally driven flow, and electroosmosis on cell-sized particle trapping under conditions of high conductance that approximates the level

found in human blood remain unknown. Further understanding the interaction between the particles and the electrokinetic device under DEP application is an essential part of validating theoretical models of DEP that can be used to improve the collection of low concentration micro- and nanosized particles from highly conductive biofluids.

Here, we used 10-μm diameter polystyrene beads as model cells because they were in the size range of cells and they had a high degree of uniformity in size and shape ensuring that differences seen in observed trajectories were not due to particle variability. The beads also provided a high level of fluorescent contrast with the background making them ideal objects for tracking. The beads differed from real cells in several ways. The beads were more spherical in morphology than real cells. The beads were more rigid than cells which can deform based on external environmental conditions. The beads were solid polystyrene and lacked the internal compartments and capacitive plasma membrane found in cells. These differences could make the magnitude of the DEP force experienced by cells different from the magnitude experienced by beads, but the electric field gradient and possible fluid flow forces present in the chip would be the same for both cells and beads. The trajectories for both are dictated largely by these factors allowing the behavior of the beads to be a model for the overall trajectory of cells.

The hydrogel layer covering the electrodes of these chips enabled DEP to be performed under high conductance conditions of 0.5× PBS (6.5 ± 0.1 mS/cm) enabling sufficient voltage application to achieve both pDEP and nDEP. These beads are known to undergo nDEP, just like cells, when exposed to a 14-kHz alternating current (AC) electric field. We compared the theoretical paths that would be taken if nDEP was the only force present with the experimentally observed paths of the particles. Large deviations from these theoretical nDEP paths would indicate influence from thermally driven convection and/or electroosmosis.

2 | MATERIALS AND METHODS

2.1 | Materials

The particles used for the nDEP experiments were FluoSpheres Polystyrene Microspheres (10-μm, yellow–green fluorescent 505/515; F8836) from Thermo Fisher Scientific. The beads were diluted to a 1:10 ratio from stock solution with 0.5× PBS. The AC signal (10 $V_{peak-to-peak}$ [V_{pp}] at 14 kHz) used for nDEP collection was produced by an Agilent 33250A 80-MHz Function/Arbitrary Waveform

Generator using a power amplifier from Newtons4th Ltd (LPA01). Three-chamber DEP chips (ExoCell EVF1P flow cell, 3-channel, EF-CRT-00002) were purchased from Biological Dynamics (San Diego, CA, USA). Beads were imaged using an Imager.D2 Zeiss microscope, and Zeiss Zen (blue edition) software was used to obtain the nDEP experiment movies.

2.1.1 | Modeling and data processing

The programs used to calculate the theoretical paths included COMSOL Multiphysics software operated in macOS Catalina Version 10.15.7, which generated the electric field simulations of the DEP chip.

JupyterLab Version 2.2.6 provided the environment for coding with Python Version 3.8.6 to perform slope tracking along the electric field gradient to determine theoretical particle paths. This utilized the scipy's spatial KDTree function and numpy. The pandas and matplotlib library were used for general data handling and plotting.

Observed experimental bead tracks were processed and overlaid on microscopy images of the electrode array using Fiji ImageJ Version 2.0.0-rc-69/1.52p [55] and its plug-in TrackMate v5.2.0 [56].

2.1.2 | Data analysis and visualization

RStudio Team (2020) Version 1.2.5 was used for plotting the data.

2.2 | nDEP collection of polystyrene beads and movie recording

The fluorescent bead sample was diluted 1:10 into 0.5× PBS from the stock solution, to avoid signal saturation, and then flowed into the DEP chip microfluidic chamber (Figure 1). Bulk fluid flow from the fluid injection was allowed to settle down and allow the particles to stop moving. An AC electric field (10 V_{pp}, 14 kHz) was then applied to the electrode array using the waveform generator and power amplifier. The electrode array and the beads were imaged from above using a D2 Zeiss microscope.

The "Movie Recorder" feature in the Zeiss Zen software was used to record the particle movement under DEP. These frames were taken under fluorescence imaging using the inherent fluorescence of the beads under GFP illumination with a 4-ms exposure time at 10 fps. The system was set to start recording 5 s prior to AC electric field application. At the 5-s mark, the AC electric field was applied for 40 s. This period of time was sufficient for
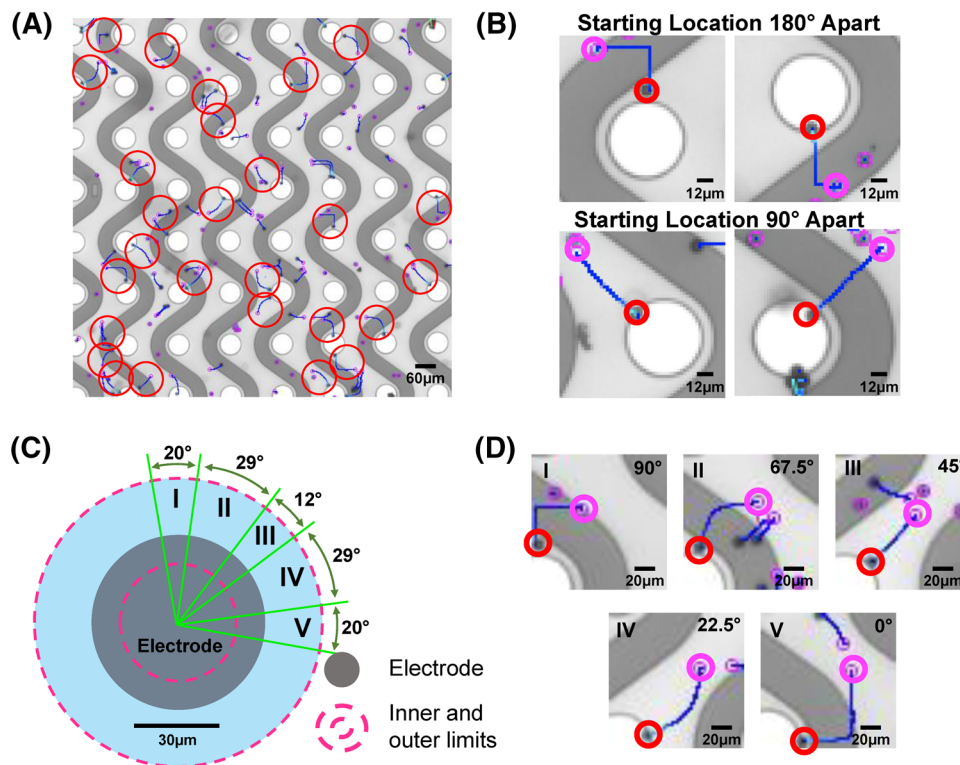
FIGURE 2 Particle selection criteria based on electrode array symmetry. (A) A bright-field top view of the DEP chip electrode array where the trajectories of the particles have been traced in TrackMate. The dark dots are the 10-μm yellow–green fluorescent beads at their starting locations. Their final collection locations are indicated by the small pink circles. (B) The quadrilateral symmetry of the electrode array resulted in particles having similar trajectories with starting locations 90° and 180° away from each other around the circular electrode. (C) Similar starting locations were grouped into angular categories defined in the positive quadrant of the electrode by the green lines. The dotted pink lines indicate the inner and outer limits of the particle inclusion zone. Each of the angular regions was labeled by the center angle: 90°, 67.5°, 45°, 22.5°, and 0°. (D) Representative particles and tracks for each of the angle categories with starting locations circled in red and their collection location circled in pink with the blue line tracing the trajectory. DEP, dielectrophoresis

particles to complete their trajectory from their random initial x,y position toward the final nDEP collection location in between the electrodes as shown in Figure 1.

2.3 | Particle tracking and particle selection criteria

Using Fiji image analysis software, the bright-field image showing the random starting location of the particles before DEP application was merged into the stacked TIFF that contained frames recorded under fluorescent GFP imaging. Merging these images established the initial position of the particles relative to the electrode location throughout the particle-tracking analysis. The images were further processed using the Fiji plugin TrackMate. This software identified the centroid of the particles and tracked their position from frame to frame drawing a line to visualize the trajectories over time as shown in Figure 2A. The individual particles inside the red circles were selected

for analysis using the criteria outlined later. The wavy light gray lines were the electrical connections between the different electrodes and were designed to allow electrodes of different polarities to sit directly next to each other in a checkerboard-like pattern.

The repeating pattern of electrodes within the array created an electric field around individual electrodes with quadrilateral symmetry, as shown in Figure 3A. This allowed us to divide the electrode into quadrants. Particles with starting locations that were 90° and 180° from one another around the electrode had similar symmetrical trajectories as shown in Figure 2B allowing us to flip and rotate the trajectories from all four quadrants toward the positive upper right quadrant of the electrode as shown in Figure 2C. This shift gave the particles a common quadrant and a shared origin allowing us to make direct comparisons between the trajectories. The origin (0,0) was set to be the centroid of the electrode setting the working environment to the positive quadrant of the electrode, as shown in Figure 2C.
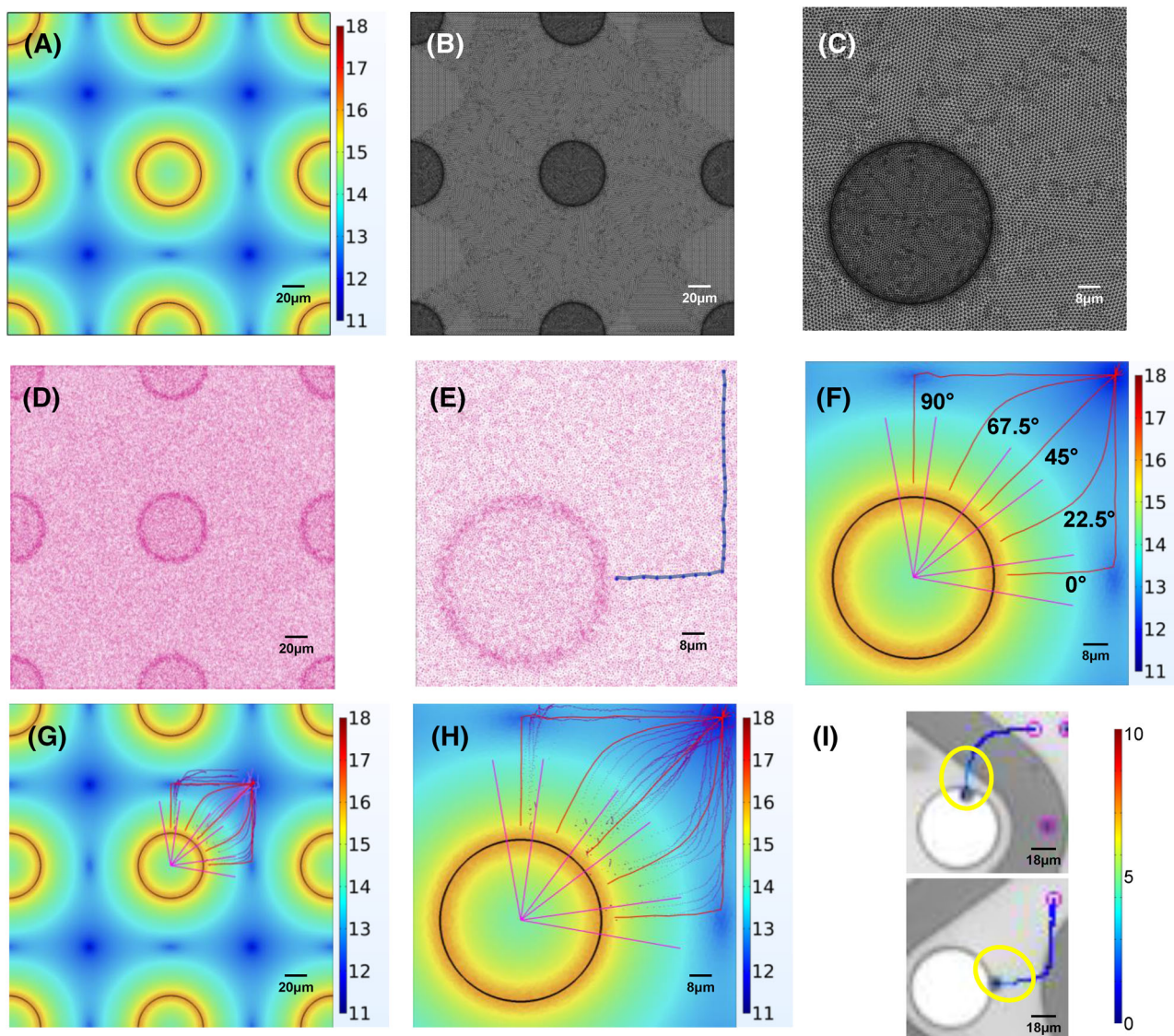
FIGURE 3 Simulation of the electric field factor $\nabla|\boldsymbol{E}|^2$ and theoretical particle trajectories. (A) A 300-μm by 300-μm top view of the DEP chip showing a COMSOL simulation of the electric field factor $\nabla|\boldsymbol{E}|^2$. The color bars here, and in F–H, represent the base-10 exponents of the electric field gradient magnitude in V^2/m^3. (B) The user defined mesh across the geometrical model of the electrode array. (C) A zoomed-in view shows the finer mesh around the electrode edges. (D) A scatterplot of the specific locations where electric field values were determined by COMSOL. (E) An example of a representative theoretical path that starts in the 0° angular category, 5 μm away from the electrode edge. (F) The electrode with the angular categories defined by the straight purple lines and the theoretical paths starting from the center of each category as the red lines. (G) A wide-field view to show how the paths fit into the larger electrode array. (H) This zoomed-in view shows the experimental tracks as the blue dotted lines following similar trajectories to the theoretical paths (red solid lines). The distances between the dots indicate that the particles moved faster in the high-field regions. (I) The velocities of the particles are color-coded along their observed path represented in pixels-traveled/frame. DEP, dielectrophoresis

Single particles were selected, avoiding particle clusters, to study individual particle movement. We selected for individual particles that had starting locations within defined inner and outer limits around the electrode edge, as shown in Figure 2C, and these starting coordinates were recorded. Particle trajectory was heavily dependent on angular starting location relative to the centroid of the electrode, so the selected particles were further organized by similarity in their angular starting position around the electrode edge (Figure 2C). The positive quadrant was divided into five angular spaces to categorize the tracks. Each angular space was labeled using the angle that passed through the center of the region. The categories were 90°, 67.5°, 45°, 22.5°, and 0°. Figure 2D shows example particle tracks from each of the five angular categories.

2.4 | Theoretical particle path calculation based on electric field gradient $\nabla|\boldsymbol{E}|^2$

COMSOL Multiphysics was used to create a finite element method (FEM) model of the electrode array to calculate the magnitude of the electric field factor $\nabla|\boldsymbol{E}|^2$ from the DEP force equation (Equation 1). This was done across a subsection of the electrode array with one complete electrode in the center and partial electrodes around it (Figure 3A). This simulation showed that the electric field intensified around the electrode edges, where pDEP collection occurred, and decreased out to the furthest points in-between the electrodes, where nDEP collection occurred.

To enable a visualization of the field, it was necessary to graph the magnitudes on a $\log_{10}$ scale. The magnitude of the electric field factor was determined in COMSOL using the following expression:

$$\log_{10}\sqrt{\left(\frac{\partial|\boldsymbol{E}|^2}{\partial x}\right)^2 + \left(\frac{\partial|\boldsymbol{E}|^2}{\partial y}\right)^2 + \left(\frac{\partial|\boldsymbol{E}|^2}{\partial z}\right)^2} \quad (2)$$

The model used $\boldsymbol{n} \cdot \boldsymbol{J} = 0$ for the boundaries above and below the plane of the electrode array where $\boldsymbol{J}$ is current density and $\boldsymbol{n}$ is the vector normal to the plane of the electrode array. The boundaries around the periphery of the electrode array subsection had a periodicity defined in COMSOL to be continuity meaning that the array subsection would repeat itself infinitely in the x and y directions to model the center of the 1000 electrode array. This prevented edge effects at the periphery of the subsection.

For the geometric structure of the model, we defined a mesh with finer elements around the electrodes to provide greater detail in these critical material boundary regions where changes in conductivity occurred (Figure 3B and C). With the COMSOL Multiphysics' FEM approach, these finer mesh sizes provided a better approximation of the electric field. In Figure 3D and E, the dots in the scatterplots show x,y coordinates where the COMSOL FEM simulation computed an electric field value (590,220 total data points). This dataset was used to calculate the theoretical particle trajectories, through slope tracking, by utilizing Python's scipy spatial KDTree nearest neighbor search and *numpy*. This process began with the starting coordinate and identified the next adjacent point with the lowest $\nabla|\boldsymbol{E}|^2$ value. This process was repeated for each subsequent point to trace a connected path from the high- to the low-field region.

Other methods exist to calculate particle motions in the environment of the DEP chip taking into account multiple different factors such as particle characteristics and theoretical fluid flow forces. We chose this slope tracking method because it allowed us to determine theoretical trajectories based only on DEP forces without influence from other factors that might be present in the chip. This enabled a direct comparison between theoretical paths from nDEP forces and observed experimental trajectories. We determined an initial starting coordinate for each of the five angular categories. This path simulated the trajectory taken by a particle experiencing only nDEP, starting near the electrode edge and being repelled toward the low-field region (Figure 3F).

3 | RESULTS AND DISCUSSION

3.1 | nDEP collection and video recording

The 10-μm diameter beads were chosen because they could be individually identified under both bright-field and fluorescent conditions, which facilitated tracking protocol development by associating individual particles with their individual tracks. To reduce the computational time for data processing, the obtained video frames showing the full view of the electrode array were cropped into four different subsections. Each subsection was handled as an individual video with a total of 16 subsections being analyzed.

3.2 | Particle tracking

As described earlier, selection criteria were applied to the particles based on their starting location to enable direct comparisons between tracks. In nDEP, the high-field regions around the electrodes repelled the particles forcing them to travel towards the low-field regions between the electrodes. After applying the particle selection criteria to the video analysis, a total of 64 particles were included in the study. We did not include particles with starting locations within the electrodes as the electric field gradient showed that this region had lower strength compared to the electrode edge and particles could get trapped inside by the surrounding high-field region at the electrode edge. In the DEP collection videos, regardless of the location that the particles started at, it was observed that the particles moved faster near the electrode edgedecreasing their velocity as they entered lower field regions. This supports the concept that the strength of the DEP force was influenced by the intensity of the electric field gradient, as shown in Figure 3H. Here a subset of the experimental trajectories was plotted showing the location of each particle from each frame of the movie as a dot . The dots were spaced further

apart from each other in the high-field region and came closer together as a particle reached the lower intensity regions of the electric field gradient. This showed that the velocity of the particles decreased after exiting the high-field region. Figure 3I shows the TrackMate paths with the velocity magnitude color-coded along the path with the yellow circles indicating where particles moved faster.

The selection criteria and angular division of space to categorize the particles suggest that the path taken by the particle when a DEP force is exerted on it is strongly dependent on the initial starting location, even if the centroids of the particles are separated by just 5 µm (Figure 4).

3.3 | Simulation of electric field gradient and simulation-based theoretical path

The model presented in Figure 3A is a representation of the electric field factor $\nabla|\boldsymbol{E}|^2$ of the DEP force equation (Equation 1) using the parameters that are set by our experiments. The theoretical paths and the example in Figure 3E inform that this model, our dataset, and our algorithm can be used to predict the DEP movement of particles from arbitrary starting points within the simulations. We found that the trajectories varied as the initial x,y location of the particle changed.

3.4 | Simulation-based calculated path comparison to experimental data

In Figure 4, the theoretical paths are plotted using thick red lines along with the experimental paths using thinner lines for each angle category. Variations in distance between the experimental and theoretical paths in each category were less than 20 µm. The quantity of experimental tracks in each category varied due to the random starting location of the particles before DEP was applied. In Figure 4F, all 64 experimental particle paths are plotted along with the theoretical path in each angle category. Together they show the symmetry of collection around the 45° angle.

The starting position of the particle was observed to heavily influence the trajectory. Particles within each angle category were observed to take similar paths due to their similar starting locations. In Figure 4A and E, the theoretical paths (thick red lines) took a sharp 90° angle on their way from the electrode edge to the global minima. Several of the experimentally observed particles took this sharp turn as well when their starting locations were closer to the starting position of the theoretical path. This sharp turn was due to a local minimum—a saddle point—directly between two electrodes that the

particles were pushed towards; this was ultimately an unstable location and the particles continued to follow the gradient to the global minima in the center among four electrodes. The observed sharpness of the turns decreased, becoming curved turns for particles in the 67.5° and 22.5° angle categories (Figure 4B and D), thus showing some influence from the local minima directly between the two electrodes. In Figure 4B, the particle starting locations for the 67.5° category were randomly all below the theoretical path (thick red line), but they all had curved trajectories similar to the theoretical path. In Figure 4C, the starting locations varied by less than 15 µm in distance, and the resulting trajectories showed that even this difference could alter the curvature of the trajectory. Particles starting closer to the 45° angle had straighter trajectories that closely followed the theoretical path and particles with starting locations further away had slight curvatures to their overall path. Figure 4D had random starting positions well dispersed above and below the theoretical path at 22.5°. Particles that had starting positions further away from the theoretical path still had similar shaped trajectories. As in the 67.5° category, the experimental paths had a curvature toward the local minima between two electrodes. In Figure 4F, all the particles are plotted in their respective angular categories with the inner and outer inclusion limits shown by purple dotted lines and the origin at the centroid of the electrode. This plot shows how important starting location was to the trajectory of the particles and how the trajectories more closely matched the theoretical path as the starting locations of the particles and theoretical paths came closer together. The solid green lines are the angle category boundaries. The dashed green line represents the 5-µm extension from the electrode edge defining the initial location of the theoretical paths.

The random starting location of each particle meant that most did not coincide directly with the starting location of the theoretical paths calculated for each angle category shown in Figure 4. Although the theoretical paths closely match the observed experimental paths, there were deviations of less than 20 µm. To understand if the observed deviations could be accounted for by the differences in particle starting location, additional theoretical paths were calculated. These theoretical paths had starting locations that bracketed the particle starting locations in each angular category, as shown in Figure 5. Here, we combined the 0° and 90° categories together (Figure 5A) as well as the 22.5° and 67.5° categories (Figure 5B) using the symmetry of the electrode array to show the full range of particle starting locations. These bracketing theoretical paths are represented by the thick red lines. The experimental particle paths mostly fell within the confines of these theoretical paths showing
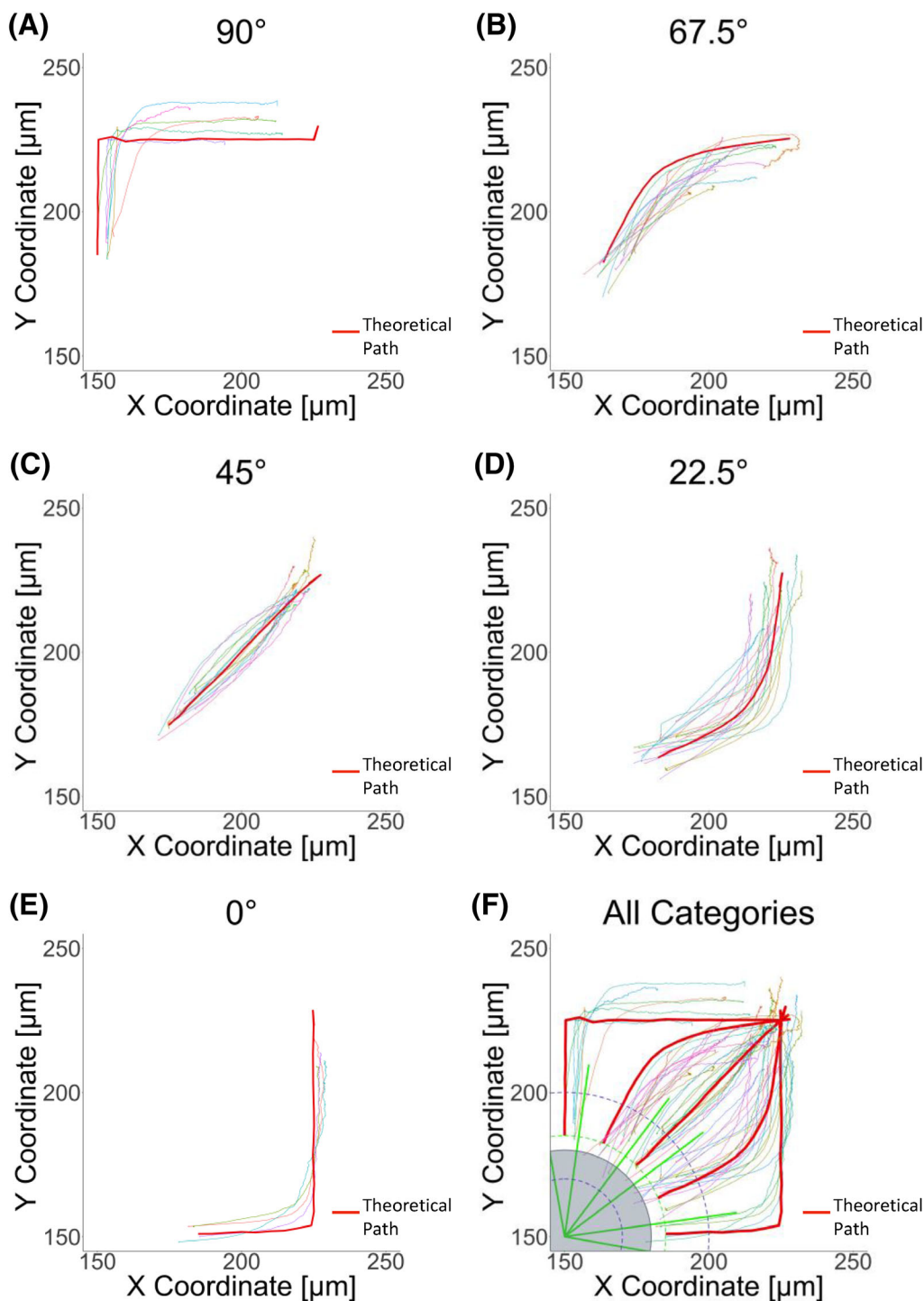
FIGURE 4 Similarities between theoretical and experimental particle tracks. The theoretical paths are shown using thick red lines and the experimental tracks are the thinner lines. These plots show the particle paths are highly influenced by their initial starting locations relative to the electrode. (A) The 90° category shows both the theoretical and the experimental trajectories taking a sharp turn near the local minima directly between two electrodes. (B) The 67.5° category shows the majority of the experimental tracks had initial locations below the starting point of the theoretical path but still had trajectories that were similar. (C) The 45° category showed a straighter trajectory toward the low-field region. (D) In the 22.5° category, some of the tracks with straighter paths showed a starting location closer to the 22.5°/45° category boundary. (E) The 0° category was similar to the 90° category. (F) A compilation of all the particle tracks in each category with their theoretical paths (thick red lines)
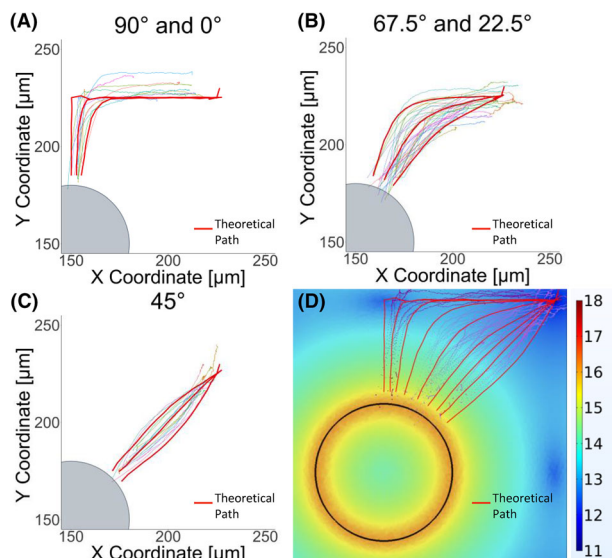
FIGURE 5 Similarity between theoretical and experimental particle trajectories. The observed variation in experimental particle trajectories within each angular category was mainly due to small variations in starting location. Theoretical paths calculated with starting locations on either side of the experimental starting locations bracketed the majority of the experimental paths. (A) Due to symmetry, the 0° and 90° angular categories were combined to show the full extent of variability. This plot includes theoretical paths in thick red that bracket the extent of experimental starting locations. (B) The experimental paths in the 67.5° and 22.5° categories were combined and largely contained by theoretical paths that bracket the experimental starting locations. (C) The bracketing theoretical paths around the 45° angle also contained the observed experimental paths. (D) An overlay of all the experimental paths (dotted blue lines) and theoretical paths (solid red lines)

that the starting location can account for the majority of this observed variability. The main variance occured with many of the particle paths extending above the theoretical paths in the 90° and 0° category and with the end point for many particles in the 67.5° and 22.5° categories ending below the theoretical location. These variances occurred in the regions of relatively low electric-field strength where the nDEP forces could move the particles close to the center of the global minimum but may not have been large enough to continue to move the particles to the very center, as shown in the upper right corner of Figure 5D.

4 | CONCLUDING REMARKS

We tracked the motion of 10-μm diameter polystyrene beads under the influence of nDEP generated by an electrode array and observed that the overall particle trajectory was highly influenced by the starting location of the bead with respect to its angular position around the nearest

circular electrode. These experimental trajectories showed that particles were repelled by the high electric field region around the electrode edge and headed toward the low-field region between electrodes. Particles from the 0° and 90° angle categories were first pushed in a straight line toward the nearest local minima of the electric field but completed their trajectory by making a sharp angled turn toward the collection region at the global minima located between four electrodes (Figure 3A). It was observed that the particles from the 22.5° and 67.5° angle categories took a slight curve likely caused by influence from the local minima between the two electrodes nearest them. Particles in the 45° category were closer to the global minima such that some experienced almost a straight-line motion toward this low-field region, arriving faster than particles from the other categories.

The experimental paths closely followed the calculated theoretical paths predicted for just the nDEP force itself. This was shown in Figure 5 where theoretical paths, with starting positions that bracketed the starting positions of the experimental beads, largely bracketed the entire set of experimental trajectories. This indicates that in these studies, nDEP was the dominant force directing particle motion and that fluid flow and effects from other phenomena, such as thermal convection and electroosmotic flow, played minimal roles in particle motion. This also indicates that the variation in experimental trajectories was mostly due to the starting location of the beads.

The observed deviations between experimental and theoretical paths in Figure 5A and B occurred in regions where the field strength was relatively low (Figure 5D), indicating there was not enough force to carry the beads all the way to the center of the global minima. Less variation was observed in the 45° angle category likely due to the direct path available to reach the global minima.

The agreement between the theoretical and the experimental paths also validates our electric field model and will enable the future addition of complexity. Moreover, the rotational symmetry of the trajectories from particles starting 90° and 180° from one another around the electrodes inform that the DEP force was consistent and stable across the electrode array.

The particle tracking and theoretical path calculation protocols developed in this study can be applied to future investigations looking at the behavior of smaller particles along with media of different conductivities, and changes to the applied voltage and frequency. Future work to determine crossover frequencies for simultaneous pDEP nanoparticle collection and nDEP cell trapping, and exploring particle velocities at different DEP parameters, could help optimize the separation of cells and circulating nanoparticles in human blood samples to enable future diagnostic applications.

CONFLICT OF INTEREST

D. Heineck is an employee of Biological Dynamics.

DATA AVAILABILITY STATEMENT

The data that support the findings of this study are available from the corresponding author upon reasonable request.

ORCID

Ramona Luna https://orcid.org/0000-0002-2957-4329
Daniel P. Heineck https://orcid.org/0000-0002-9336-1256
Elmar Bucher https://orcid.org/0000-0002-2929-2460
Laura Heiser https://orcid.org/0000-0003-3330-0950
Stuart D. Ibsen https://orcid.org/0000-0001-8619-3832

REFERENCES

1. Mu X, Zheng W, Sun J, Zhang W, Jiang X. Microfluidics for manipulating cells. Small. 2013;9:9–21.
2. Guo F, French JB, Li P, Zhao H, Chan CY, Fick JR, et al. Probing cell-cell communication with microfluidic devices. Lab Chip. 2013;13:3152–62.
3. Benavente-Babace A, Gallego-Pérez D, Hansford DJ, Arana S, Pérez-Lorenzo E, Mujika M. Single-cell trapping and selective treatment via co-flow within a microfluidic platform. Biosens Bioelectron. 2014;61:298–305.
4. Frimat J-P, Becker M, Chiang Y-Y, Marggraf U, Janasek D, Hengstler JG, et al. A microfluidic array with cellular valving for single cell co-culture. Lab Chip. 2011;11:231–7.
5. Kang S-M, Kim D, Lee J-H, Takayama S, Park JY. Engineered microsystems for spheroid and organoid studies. Adv Healthcare Mater. 2021;10:2001284.
6. Schwarzenbach H, Hoon DS, Pantel K. Cell-free nucleic acids as biomarkers in cancer patients. Nat Rev Cancer. 2011;11:426–37.
7. Melo SA, Luecke LB, Kahlert C, Fernandez AF, Gammon ST, Kaye J, et al. Glypican-1 identifies cancer exosomes and detects early pancreatic cancer. Nature. 2015;523:177–82.
8. Turcan I, Olariu MA. Dielectrophoretic manipulation of cancer cells and their electrical characterization. ACS Comb Sci. 2020;22:554–78.
9. An M, Lohse I, Tan Z, Zhu J, Wu J, Kurapati H, et al. Quantitative proteomic analysis of serum exosomes from patients with locally advanced pancreatic cancer undergoing chemoradiotherapy. J Proteome Res. 2017;16:1763–72.
10. Whiteside TL. Tumor-derived exosomes and their role in cancer progression. Adv Clin Chem. 2016;74:103–41.
11. Di Carlo D, Wu LY, Lee LP. Dynamic single cell culture array. Lab Chip. 2006;6:1445–9.
12. Liu W, Li L, Wang JC, Tu Q, Ren L, Wang Y, et al. Dynamic trapping and high-throughput patterning of cells using pneumatic

microstructures in an integrated microfluidic device. Lab Chip. 2012;12:1702–9.
13. Jin D, Deng B, Li JX, Cai W, Tu L, Chen J, et al. A microfluidic device enabling high-efficiency single cell trapping. Biomicrofluidics. 2015;9:014101.
14. Jang K, Sato K, Mawatari K, Konno T, Ishihara K, Kitamori T. Surface modification by 2-methacryloyloxyethyl phosphorylcholine coupled to a photolabile linker for cell micropatterning. Biomaterials. 2009;30:1413–20.
15. Antfolk M, Laurell T. Continuous flow microfluidic separation and processing of rare cells and bioparticles found in blood – a review. Anal Chim Acta. 2017;965:9–35.
16. Brooks AR, Lelkes PI, Rubanyi GM. Gene expression profiling of vascular endothelial cells exposed to fluid mechanical forces: relevance for focal susceptibility to atherosclerosis. Endothelium. 2004;11:45–57.
17. Wasserman SM, Mehraban F, Komuves LG, Yang RB, Tomlinson JE, Zhang Y, et al. Gene expression profile of human endothelial cells exposed to sustained fluid shear stress. Physiol Genomics. 2002;12:13–23.
18. Avvisato CL, Yang X, Shah S, Hoxter B, Li W, Gaynor R, et al. Mechanical force modulates global gene expression and beta-catenin signaling in colon cancer cells. J Cell Sci. 2007;120(Pt 15):2672–82.
19. Pohl HA. The motion and precipitation of suspensoids in divergent electric fields. J Appl Phys. 1951;22:869–71.
20. Sarno B, Heineck D, Heller MJ, Ibsen SD. Dielectrophoresis: developments and applications from 2010 to 2020. Electrophoresis. 2021;42:539–64.
21. Gustafson KT, Katherine TH, Daniel H, Jesus B, Augusta M, Sejung K, Austin G, Randall A, Carolyn ES, Stuart DIbsen. Automated fluorescence quantification of extracellular vesicles collected from blood plasma using dielectrophoresis. Lab on a Chip. 2021;21:1318–1332.
22. Qian C, Huang H, Chen L, Li X, Ge Z, Chen T, et al. Dielectrophoresis for bioparticle manipulation. Int J Mol Sci. 2014;15:18281–309.
23. Pethig R. Dielectrophoresis: theory, methodology and biological applications. Hoboken, NJ: John Wiley & Sons; 2017.
24. Wei MT, Junio J, Ou-Yang HD. Direct measurements of the frequency-dependent dielectrophoresis force. Biomicrofluidics. 2009;3:12003.
25. Nejad HR, Chowdhury OZ, Buat MD, Hoorfar M. Characterization of the geometry of negative dielectrophoresis traps for particle immobilization in digital microfluidic platforms. Lab Chip. 2013;13:1823–30.
26. Velev OD, Gangwal S, Petsev DN. Particle-localized AC and DC manipulation and electrokinetics. Annu Rep Sect C (Phys Chem). 2009;105:213–46.
27. Ibsen SD, Wright J, Lewis JM, Kim S, Ko SY, Ong J, et al. Rapid isolation and detection of exosomes and associated biomarkers from plasma. ACS Nano. 2017;11:6641–51.
28. Lewis JM, Vyas AD, Qiu Y, Messer KS, White R, Heller MJ. Integrated analysis of exosomal protein biomarkers on alternating current electrokinetic chips enables rapid detection of pancreatic cancer in patient blood. ACS Nano. 2018;12:3311–20.
29. Mathew B, Alazzam A, Abutayeh M, Gawanmeh A, Khashan S. Modeling the trajectory of microparticles subjected to dielectrophoresis in a microfluidic device for field flow fractionation. Chem Eng Sci. 2015;138:266–80.

30. Alnaimat F, Ramesh S, Adams S, Parks N, Lewis C, Wallace K, et al. Model-based performance study of dielectrophoretic flow separator. IEEE Sens Lett. 2019;3:4500504.

31. BI MZA, Tirth V, Yousuff CM, Shukla NK, Islam S, Irshad K, et al. Simulation guided microfluidic design for multitarget separation using dielectrophoretic principle. BioChip J. 2020;14:390–404.

32. Sun H, Ren Y, Hou L, Tao Y, Liu W, Jiang T, et al. Continuous particle trapping, switching, and sorting utilizing a combination of dielectrophoresis and alternating current electrothermal flow. Anal Chem. 2019;91:5729–38.

33. Song H, Rosano JM, Wang Y, Garson CJ, Prabhakarpandian B, Pant K, et al. Continuous-flow sorting of stem cells and differentiation products based on dielectrophoresis. Lab Chip. 2015;15:1320–8.

34. Moon H-S, Kwon K, Kim S-I, Han H, Sohn J, Lee S, et al. Continuous separation of breast cancer cells from blood samples using multi-orifice flow fractionation (MOFF) and dielectrophoresis (DEP). Lab Chip. 2011;11:1118–25.

35. Yang F, Zhang Y, Cui X, Fan Y, Xue Y, Miao H, et al. Extraction of cell-free whole blood plasma using a dielectrophoresis-based microfluidic device. Biotechnol J. 2019;14:1800181.

36. Ibsen S, Sonnenberg A, Schutt C, Mukthavaram R, Yeh Y, Ortac I, et al. Recovery of drug delivery nanoparticles from human plasma using an electrokinetic platform technology. Small. 2015;11:5088–96.

37. Heineck DP, Sarno B, Kim S, Heller M. Electrochemical attack and corrosion of platinum electrodes in dielectrophoretic diagnostic devices. Anal Bioanal Chem. 2020;412:3871–80.

38. Huang Y, Pethig R. Electrode design for negative dielectrophoresis. Meas Sci Technol. 1991;2:1142.

39. Park S, Koklu M, Beskok A. Particle trapping in high-conductivity media with electrothermally enhanced negative dielectrophoresis. Anal Chem. 2009;81:2303–10.

40. Abd Rahman N, Ibrahim F, Yafouz B. Dielectrophoresis for biomedical sciences applications: a review. Sensors. 2017;17:449.

41. Kwak TJ, Hossen I, Bashir R, Chang W-J, Lee CH. Localized dielectric loss heating in dielectrophoresis devices. Sci Rep. 2019;9:18977.

42. Du F, Baune M, Thöming J. Insulator-based dielectrophoresis in viscous media—simulation of particle and droplet velocity. J Electrostat. 2007;65:452–8.

43. Seelig T, Meyer A, Gerstner P, Meier M, Jongmanns M, Baumann M, et al. Dielectrophoretic force-driven convection in annular geometry under Earth's gravity. Int J Heat Mass Transfer. 2019;139:386–98.

44. Yoshikawa HN, Crumeyrolle O, Mutabazi I. Dielectrophoretic force-driven thermal convection in annular geometry. Phys Fluids. 2013;25:024106.

45. Turnbull R. Effect of dielectrophoretic forces on the Bénard instability. Phys Fluids. 1969;12:1809–15.

46. Chandra B, Smylie D. A laboratory model of thermal convection under a central force field. Geophys Fluid Dyn. 1972;3:211–24.

47. Kunti G, Agarwal T, Bhattacharya A, Maiti TK, Chakraborty S. On-chip concentration and patterning of biological cells using interplay of electrical and thermal fields. Anal Chem. 2020;92:838–44.

48. Dalili A, Taatizadeh E, Tahmooressi H, Tasnim N, Rellstab-Sánchez PI, Shaunessy M, et al. Parametric study on the geometrical parameters of a lab-on-a-chip platform with tilted planar electrodes for continuous dielectrophoretic manipulation of microparticles. Sci Rep. 2020;10:11718.

49. Koklu A, Sabuncu AC, Beskok A. Enhancement of dielectrophoresis using fractal gold nanostructured electrodes. Electrophoresis. 2017;38:1458–65.

50. Gagnon Z, Chang HC. Aligning fast alternating current electroosmotic flow fields and characteristic frequencies with dielectrophoretic traps to achieve rapid bacteria detection. Electrophoresis. 2005;26:3725–37.

51. Asbury CL, van den Engh G. Trapping of DNA in nonuniform oscillating electric fields. Biophys J. 1998;74:1024–30.

52. Gencoglu A, Olney D, LaLonde A, Koppula KS, Lapizco-Encinas BH. Dynamic microparticle manipulation with an electroosmotic flow gradient in low-frequency alternating current dielectrophoresis. Electrophoresis. 2014;35:362–73.

53. Martínez-López JI, Moncada-Hernández H, Baylon-Cardiel JL, Martínez-Chapa SO, Rito-Palomares M, Lapizco-Encinas BH. Characterization of electrokinetic mobility of microparticles in order to improve dielectrophoretic concentration. Anal Bioanal Chem. 2009;394:293–302.

54. Castellanos A, Ramos A, Gonzalez A, Green NG, Morgan H. Electrohydrodynamics and dielectrophoresis in microsystems: scaling laws. J Phys D: Appl Phys. 2003;36:2584.

55. Schindelin J, Arganda-Carreras I, Frise E, Kaynig V, Longair M, Pietzsch T, et al. Fiji: an open-source platform for biological-image analysis. Nat Methods. 2012;9:676–82.

56. Tinevez J-Y, Perry N, Schindelin J, Hoopes GM, Reynolds GD, Laplantine E, et al. TrackMate: an open and extensible platform for single-particle tracking. Methods. 2017;115:80–90.